CHEMISTRY OF MATERIALS

Article

pubs.acs.org/cm

Tailoring Mesoporous γ-Al_2O_3 Properties by Transition Metal Doping: A Combined Experimental and Computational Study

Liangjie Fu,[†,‡] Huaming Yang,*[,†] Yuehua Hu,[†] Di Wu,*[,§] and Alexandra Navrotsky*[,‡]

[†]Centre for Mineral Materials, School of Minerals Processing and Bioengineering, Central South University, Changsha, Hunan 410083, China

[‡]Peter A. Rock Thermochemistry Laboratory and NEAT ORU, University of California Davis, One Shields Avenue, Davis, California 95616, United States

[§]The Gene and Linda Voiland School of Chemical Engineering and Bioengineering, Department of Chemistry, Materials Science and Engineering, Washington State University, Pullman, Washington 99163, United States

Supporting Information

ABSTRACT: Well crystallized gamma alumina (γ-Al_2O_3) with high thermal stability is as an important catalyst support. A series of first row transition metal (TM) doped aluminas with ordered mesoporous structures and homogeneous distribution of TM in the bulk structure has been synthesized by a one-pot method. The structures are studied by powder X-ray diffraction (XRD) and transmission electron microscopy (TEM), while the electronic properties are explored by X-ray photoelectron spectroscopy (XPS), valence band XPS, and UV−vis spectra. To explore the influence of TM dopants on atomistic properties (bond length, charge state, band edge, and redox properties) of γ-Al_2O_3, the cation distribution of TM dopants is studied in detail by combining experiments and density functional theory (DFT) calculations. The cooperative effect of TM dopants and intrinsic defects in γ-Al_2O_3 induces a doping mechanism distinct from that in other spinel oxides; the concentration of Al vacancies (V_{Al}) decreases with increasing atomic number of the TM dopant as a result of charge compensation effects. Such variation could be used to tailor the properties and alter the reactivity of γ-Al_2O_3.

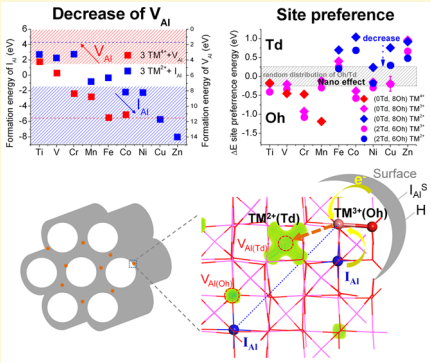

INTRODUCTION

The defect spinel alumina, γ-Al_2O_3, which has lower surface energy than α-Al_2O_3 and becomes thermodynamically stable at surface areas greater than 75 m^2/g,[1] is an important support material in industry. Since the morphology and acid−base characteristics of alumina are beneficial in various catalytic applications, such as petroleum refining, automobile emission control, and environmental remediation,[2−4] there has been great interest in obtaining well-defined mesoporous aluminum oxides (MA) with high surface area and pore volume.[5−11] The γ-alumina support, inherently inert as an unreducible oxide but a good host for reactive catalytic materials, can replace other supports in many fields. For example, the more active character of Au_n/Al_2O_3 over Au_n/TiO_2 for partial oxidation of propene was demonstrated.[12]

Catalysis by doped oxides is an emerging field.[13] It is well-known that the structural and electronic properties of reducible metal oxides such as TiO_2,[14−16] ZnO,[14,17−21] and CeO_2 can be tailored by doping of various metal elements. To improve support performance, doping of transition metal (TM) ions, such as Ti,[22] Cr,[23] Mn,[24,25] Fe,[26] Co,[27−29] Ni,[27,30] Cu,[27,31] and Zn,[32] in alumina has been carried out. Recently, the successful preparation of mesoporous alumina (MA)[33] has enabled one-pot synthesis of TM doped alumina with well-developed mesoporosity. The one-pot method gives homogeneously distributed metal dopants in the alumina structure and inhibits the aggregation of metal dopants as well as the formation of metal oxides or metal aluminate spinels.[34−36] Such doping, throughout the material rather than just at its surface, will alter the thermal stability, isoelectric point, and electronic properties. Such ordered mesoporous alumina with controllable pore size exhibits size selectivity for different molecules,[33] and its thermal stability increases with metal doping.[35] It is expected that the well dispersed metal dopants in mesoporous γ-Al_2O_3 will modify the intrinsic properties of the alumina support and may play a similar role as Mo/Cr charge donors in CaO/MgO adsorbed on gold.[37] Various dopants, such as Mg, Ca, Ni, Ti, Cr, and K, were explored recently,[35,38−40] and inorganic salts were also used as precursors.[36] However, the detailed geometric and electronic structures of these materials are still poorly known.

Decades ago, the cation distribution in spinels was discussed in terms of crystal field theory, and the orbital splitting was determined from optical and magnetic data.[41] After the development of thermodynamic models for the cation distribution,[42−44] a simple point-ion electrostatic model was

Received: November 28, 2016
Revised: January 6, 2017
Published: January 8, 2017

DOI: 10.1021/acs.chemmater.6b05041
Chem. Mater. 2017, 29, 1338−1349

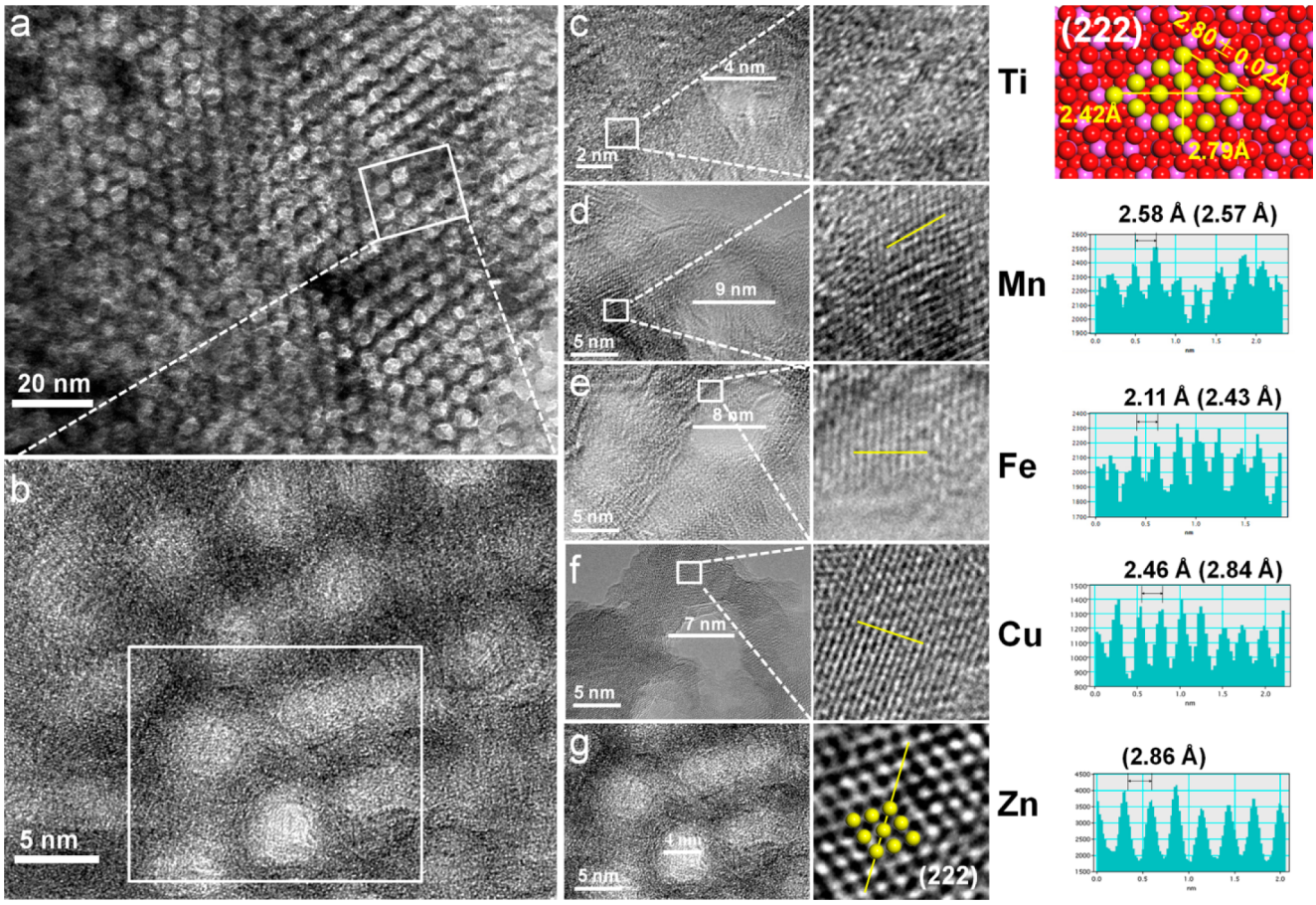

Figure 1. Morphology and structure of some MA-7TM samples. (a) TEM image and (b) amplified image show the mesoporous structure of MA-7Zn. HRTEM images show the mesopores and lattice structures for (c) MA-7Ti, (d) MA-7Mn, (e) MA-7Fe, (f) MA-7Cu, and (g) MA-7Zn. The corresponding normalized image intensities and the average *d* (Å) at three directions on (222) surface are given. The numbers in brackets are the nearest O−O distance.

proposed to explain the cation distribution.[45] The doping rules in spinel oxides were studied using an inverse design approach.[46] However, quantitative analysis of the cation distribution for metal doping in γ-Al_2O_3 is still an unresolved challenge due to the high concentration of defects, especially cation vacancies. Recently, combined with experimental analysis, we reexamined the structure of γ-Al_2O_3 using density functional theory (DFT) calculations, and the doping mechanism in the defect spinel structure was found to be more complicated than that in other oxides.[34]

In this work, a series of TM-doped γ-Al_2O_3 phases with ordered mesoporous structures has been synthesized and characterized. The TM doping configurations and the influence of TM doping on intrinsic defects are discussed on the basis of DFT calculations. The cation distribution and the energetically favorable structures are clarified by combining the computational and experimental observations. The analysis of electronic structure, combining experimental characterization and DFT calculations, indicates that the charge compensation effects, nanoscale effects, and orbital splitting under different cation distribution (octahedral (Oh) site or tetrahedral (Td) site, well dispersed or aggregated, bulk or surface) are the key factors for the doping mechanism. As a result, the cation vacancy concentration decreases with increasing atomic number of the TM dopant and the electronic structure and optical properties of γ-Al_2O_3 can be tuned by the well dispersed TM dopants.

■ EXPERIMENTAL METHODS

Synthesis. Mesoporous Al_2O_3 samples were synthesized as previously described.[34] Transition metal-doped mesoporous Al_2O_3 (MA-7TM, T = Ti, V, Cr, Mn, Fe, Co, Ni, Cu, and Zn) samples were synthesized using a series of metal precursors. 2.0 g of pluronic P_{123} or F127 (Sigma-Aldrich) was dissolved in ethanol (20 mL) under stirring for 3 h to obtain solution 1. 0.84 g of citric acid (99.5%, Sinopharm Chemical Reagent Co., Ltd.), 7.0 g of $Al(NO_3)_3{\cdot}9H_2O$ (99.5%, Sinopharm Chemical Reagent Co., Ltd.), and a small amount of transition metal precursors were added into ethanol solution stepwise under vigorous stirring to obtain solution 2. The following different types of metal precursors were used for each doping element: $TiCl_4$, $C_{10}H_{14}O_5V$, $CrCl_3{\cdot}6H_2O$, $MnSO_4{\cdot}H_2O$, $Fe(NO_3)_3{\cdot}9H_2O$/$FeSO_4{\cdot}7H_2O$, $Co(CH_3COO)_2{\cdot}4H_2O$/$CoSO_4{\cdot}7H_2O$, $NiCl_2{\cdot}6H_2O$, $Cu(CH_3COO)_2{\cdot}H_2O$/$CuCl_2{\cdot}2H_2O$, or $Zn(NO_3)_2{\cdot}6H_2O$ (99.5%, Sinopharm Chemical Reagent Co., Ltd.). TM/(TM + Al) values were controlled to be 7 at % except that of MA-7(Cr + Zn), which was synthesized using a 1:1 Cr to Zn ratio. Solution 2 was transferred to solution 1, and 10.0 mL of ethanol was used to maximize the transfer of metal precursors. The combined solution was covered with polyethylene film and stirred for 5 h. The final solution was subjected to slow evaporation at 60 °C in an oven for 3 days.

Characterization. Powder X-ray diffraction (XRD) patterns were collected using a D/MAX2550VB+ X-ray diffractometer (Cu Kα, 2° per min). Structural analysis was conducted by XRD using a Bruker D8 diffractometer (Cu Kα, 40 kV, 30 mA). The sample was rotated at 15 rpm during data collection. Lattice parameters and crystallite sizes were calculated by whole pattern fitting as implemented in Jade MDI 6.1 (Materials Data, Inc., Livermore, CA). N_2 adsorption−desorption

DOI: 10.1021/acs.chemmater.6b05041
Chem. Mater. 2017, 29, 1338−1349

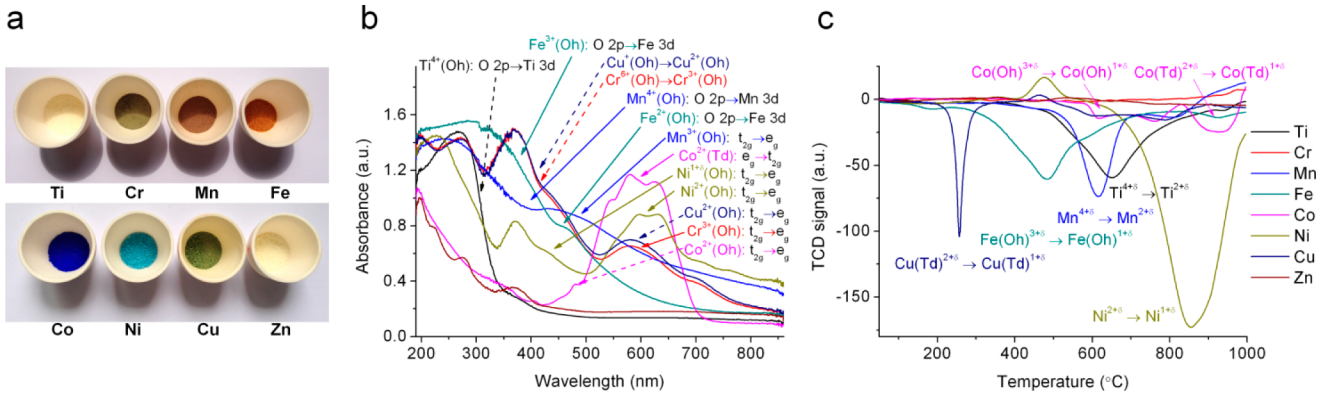

Figure 2. (a) Color, (b) UV−vis spectra, and (c) H_2-TPR profiles of MA-7TM samples.

isotherms were measured at −196 °C using a Micromeritics ASAP 2010 adsorption analyzer. BET surface areas were determined from the linear region of the BET plot (adsorption data in 0.05−0.30 range of relative pressures). Pore size distributions were calculated from the desorption isotherms by the Barrett−Joyner−Halenda (BJH) model. Transmission electron microscopy (TEM) images were recorded using a Tecnai G220ST electron microscopy operated at 200 kV. X-ray photoelectron spectroscopy (XPS) spectra were collected using an VG Multilab 2000 Spectrometer with Al Kα radiation (1486.6 eV). UV−vis diffuse reflectance spectra were measured using a TU-1901 spectrophotometer equipped with an integrating sphere attachment (IS 19−1). H_2-TPR was performed on a FineSorb 3010 adsorption system (Finetec, China). Sample was pretreated in an argon flow of 30 mL/min at 120 °C for 70 min and then cooled to room temperature. TPR experiments were carried out in 10% H_2/Ar (30 mL/min) increasing the temperature from room temperature to 1000 °C (12 °C/min). The H_2 consumption was monitored by a thermal conductivity detector (TCD).

Computation. All calculations were carried out using the CASTEP program (Cambridge Sequential Total Energy Package)[47] based on density functional theory (DFT). The generalized gradient approximation (GGA) with the exchange-correlation potential by Perdew, Burke, and Ernzerhof (PBE)[48] was used in our calculations. Ultrasoft pseudopotential plane wave formalism was applied for efficient computation. An energy cutoff of 400 eV was used. Monkhorst-Pack grids with 1 × 3 × 3 k points were used to calculate the accurate density of electronic states for 3 × 1 × 1 supercell of γ-Al_2O_3 and 1 × 2 × 2 k points for 3 × $\sqrt{2}$ × $\sqrt{2}$ supercell. Similar density of k-points was used for the pristine supercell of transition metal oxide and spinel oxide. The self-consistent total energy in the ground state was effectively achieved by the density-mixing scheme. The convergence threshold for self-consistent field (SCF) tolerance was set to be 1.0 × 10^{-6} eV/atom. The elements investigated in valence states are O($2s^2 2p^4$), Al($3s^2 3p^1$), Ti($3s^2 3p^6 3d^2 4s^2$), V($3s^2 3p^6 3d^3 4s^2$), Cr($3s^2 3p^6 3d^5 4s^1$), Mn($3d^5 4s^2$), Fe($3d^6 4s^2$), Co($3d^7 4s^2$), Ni($3d^8 4s^2$), Cu($3d^{10} 4s^1$), and Zn($3d^{10} 4s^2$). We applied uspcc pseudopotentials for Mn, Fe, Co, and Ni, while usp pseudopotentials were used for the rest of the elements after testing. In geometry optimizations, all forces applied on the atoms were converged to be less than 0.03 eV/ Å. The total stress tensor was reduced to the order of 0.05 GPa, while the maximum ionic displacement was limited within 0.001 Å.

■ RESULTS AND DISCUSSION

Structure and Morphology. The mesoporous γ-Al_2O_3 structures were obtained by using different types of transition metal salt precursors. For each doping element, the samples using different transition metal precursors (not shown) or surfactants results in similar color (Figure S1). According to the small-angle XRD (SAXRD) patterns (Figure S2), after TM doping, all TM doped γ-Al_2O_3 (MA-7TM) (except V doped γ-Al_2O_3) maintain the ordered 2D mesostructures with the spinel alumina lattice showing one very strong peak at about 0.7° and two broad signals at 1.6° and 2.0°. These peaks are characteristics of the wormhole-like mesostructures (also see the TEM image, Figure 1a) with high surface area (Table S1).

N_2 adsorption−desorption on MA-7TM results in type IV isotherms with sharp-rising, relatively narrow hysteresis loops for all samples (see Figure S3), indicating relatively narrow pore size distribution and open pore connectivity, and well-defined mesoporosity. The HRTEM images demonstrate that the highly ordered mesoporous structures are maintained upon TM doping (Figure 1b). Although narrow pore-size distribution is achieved for each MA-7TM, slight alteration of pore size is observed as the TM dopant varies (Figure 1c−g). It is observed that the mesostructure of MA-7TM varies with detailed synthesis conditions (the calcination procedures, the type of surfactant,[33] aluminum precursor,[33] and other metal precursors[35,36,40]) as reported previously. Normally, the one-pot method gives mesoporous alumina (MA) with surface area decreasing with calcinations temperature and hold time, resulting in the formation of amorphous alumina with surface area of 300−400 m^2/g (held at 400 °C for 4 h) or γ-alumina with surface area of 150−250 m^2/g (held at 900 °C for 1 h).[33] Doping with other metal atoms at around 10 at % also leads to a decrease of surface area to about 100 m^2/g.[35] The XRD patterns confirm spinel structures of MA-7TM samples (Figure S2). The MA-7TM samples possess strong reflections compared with pure MA and the crystallinities are similar, except for MA-7Ti, which is more poorly crystallized. We attribute this to the increase of lattice vacancies under charge compensation effect, as supported by DFT calculations in next section. The crystallite sizes of MA-7TM give a trend of MA-7Ti < MA-7Cr ≈ MA ≈ MA-7Fe < MA-7Mn ≈ MA-7Cu < MA-7Ni ≈ MA-7Co ≈ MA-7Zn. However, the surface crystallinity of some MA-7TM samples shows the trend as MA-7Ti < MA-7Mn ≈ MA-7Fe < MA-7Cu ≈ MA-7Zn. The surface lattice constants obtained from HRTEM for these samples varies in a different way than the bulk lattice constants from XRD using whole pattern fitting procedures (Table S1).

Spectroscopic Studies. The MA-7TM samples exhibit characteristic colors and different optical absorption properties (Figure 2a,b). While pure MA shows a band gap of around 3.5 eV[49] with absorption edge similar to commercial γ-Al_2O_3, MA-7TM samples show several absorption bands around 200−350, 350−500, and 500−750 nm. While the absorptions in the first range are attributed to interband transitions (extended adsorption edges), the absorptions in the second range are mostly ligand−metal charge transfer (O 2p to TM 3d orbitals),

DOI: 10.1021/acs.chemmater.6b05041
Chem. Mater. 2017, 29, 1338−1349

Table 1. Binding Energy (eV) and Calculated Mulliken Charge (e) of TM in Corresponding Metal Oxides (MO), Spinel Oxides, and MA-7TM Samples[a]

	Ti	Cr	Mn	Fe	Co	Ni	Cu	Zn
MO	TiO_2	CrO_3	MnO_2					
	Ti_2O_3	CrO_2	Mn_2O_3	Fe_2O_3	Co_2O_3			
		Cr_2O_3	Mn_3O_4	Fe_3O_4	Co_3O_4	Ni_2O_3	CuO	
			MnO	FeO	CoO	NiO	Cu_2O	ZnO
			$MnAl_2O_4$	$FeAl_2O_4$	$CoAl_2O_4$	$NiAl_2O_4$	$CuAl_2O_4$	$ZnAl_2O_4$
binding energy in MO[61]	458.5	579.5	642.6					
	456.8	577.0	641.7	711.3	781.3			
		576.0	641.1−641.9	710.8	780.7	855.8−856.0	933.9	
			640.8	709.6	780.2	855.0	932.7	1021.5
			641.30	**710.0**	**780.6−781.1**	**855.9−857.0**	**934.7−935.0**	**1021.7**
charge in MO	1.33	1.16	1.05					
	1.02	1.03	0.98	1.11	0.85			
		0.92	0.91(Td), 0.91(Oh)	0.99(Td), 0.93(Oh)	0.71(Td), 0.83(Oh)	/	0.62	
			0.80	0.75	0.72	0.63	0.33	0.82
			/	**0.86(Td)**	**0.83(Td)**	**0.65−0.73**	**0.75(Td)**	**0.80(Td)**
binding energy in MA-7TM	458.5	577.0−579.0	641.5−642.5	**711.3−712.3**	**781.7**	**856.5**	**933.6−934.6**	**1022.2**
charge of TM^{Z+} (Z = 4, 3, 2, 1) in MA-7TM	**1.46(Oh)**	1.24(Oh)	1.06(Td), 1.14(Oh)					
	1.28(Oh)	**1.16(Oh)**	1.04(Td), **1.13(Oh)**	1.13(Td), **1.20(Oh)**	0.90(Td), 0.96(Oh)	0.89(Oh)		
			0.96(Td), /	0.90(Td), 0.96(Oh)	**0.82(Td)**, 0.87(Oh)	**0.78(Oh)**	0.73(Td), **0.81(Oh)**	**0.90(Td)**
							0.36(Td), **0.58(Oh)**	
oxidation state of TM in MA-7TM	**Ti^{4+}**	Cr^{4+}	Mn^{4+}					
	Ti^{3+}	**Cr^{3+}**	**Mn^{3+}**	**Fe^{3+}**	Co^{3+}	Ni^{3+}		
				Fe^{2+}	**Co^{2+}**	**Ni^{2+}**	**Cu^{2+}**	**Zn^{2+}**
							Cu^{1+}	

[a]The oxidation states of TM in MA-7TM samples as deduced by comparing the calculated Mulliken charge (e) and binding energy (eV).

and the last are attributed to the intraband d−d transitions ($TM^{(z\pm\delta)+}$ ions in Oh or Td coordination). It is well-known that TM doping in oxides such as TiO_2, ZnO,[50] and other oxides[51−53] will introduce various optical absorption bands in the visible range. Though the absorption bands of TM in γ-Al_2O_3 are different from those in corundum,[54] some well-known bands for Cr^{3+}, Co^{2+}, and Ni^{2+} in spinel oxides[55] can be identified (Figure 2b, solid arrows). The color evolution (related to electronic structure evolution) for the bulk doped samples is distinctively different from that in surface doped samples.[31,38,56,57]

The valence states of TM in MA-7TM samples are studied by XPS analysis (Table 1, Figure S4). For the MA-7Ti sample, the XPS Ti 2p core level is observed at 458.5 eV (Ti 2p3/2) and 464.2 eV (Ti 2p1/2), which is characteristic of Ti^{4+}.[58] This corresponds well with results from the PLA method.[22] No Ti^{3+} species are observed, consistent with synthesis in an oxidizing atmosphere. The major peaks of Cr 2p3/2 binding energies are similar to those of Cr doped γ-Al_2O_3,[57,59] and the peaks from 579.0 to 577.0 eV can be assigned to Cr^{6+}, Cr^{4+}, and Cr^{3+}, respectively. The Mn 2p3/2 signals at 641.5 and 642.5 eV can be assigned to Mn^{3+} and Mn^{4+} in their oxides[25] or otherwise assigned as the Mn^{2+} and Mn^{3+} in spinel oxides. When TM is Fe or Co, assignment of the two 2p3/2 peaks is less clear. These peaks were reported to be either TM^{3+}/TM^{2+} or TM(Oh)/TM(Td).[26,28,60] The Ni 2p3/2 binding energies at 856.5 eV are characteristics of Ni^{2+} in the spinel structure.[30] The Cu 2p3/2 peaks at about 933.6 and 934.6 eV are characteristic of Cu^{+} and Cu^{2+} in γ-Al_2O_3 as reported previously.[34] The Zn 2p3/2 signal at 1022.2 eV is attributed to Zn^{2+}.[32]

According to the Al 2p and O 1s XPS signals in XPS spectra, for the MA-7TM sample, there appear to be slight shifts relative to undoped MA, from 74.4 to 74.0 eV for Al 2p and from 531.2 to 530.8 eV for O 1s (Figure S5). Mn doping increases the binding energy of Al while Ti or Zn decreases it. Cr, Mn, Co, Ni, or Cu doping increases the binding energy of O while Ti or Zn decreases it. Such phenomena probably suggest that, compared to pure MA, the chemical states of Al and O atoms in MA-7TM may partially self-balance to fine-tune their local environments in which electrons are donated or accepted upon substitution of Al^{3+} by TM.

Temperature-programmed reduction (H_2-TPR) experiments were performed. The TPR profiles for pure transition metal oxide (TMO) or supported TMO have already been widely studied, and the reduction temperature varies with TMO type, crystallite size, and their interaction with γ-Al_2O_3 support.[56,59,62] Compared to the surface doped case, the reduction abilities of MA-7TM catalysts are highly influenced by the homogeneously distributed TM dopants, showing a narrow reduction temperature range (Figure 2c). The reduction temperature is also elevated by the incorparation of TM into the structure, which also results in the lack of reduction of Cr in contrast to the surface supported case.[59]

Computational Results. *Structure.* γ-Al_2O_3 is a nanophase with typical crystallite size of 10 to 100 Å. Due to the poor crystallinity of γ-Al_2O_3, the exact crystallographic structure, whether spinel[34,63−66] or nonspinel,[67,68] was in debate. Since

DOI: 10.1021/acs.chemmater.6b05041
Chem. Mater. 2017, 29, 1338−1349

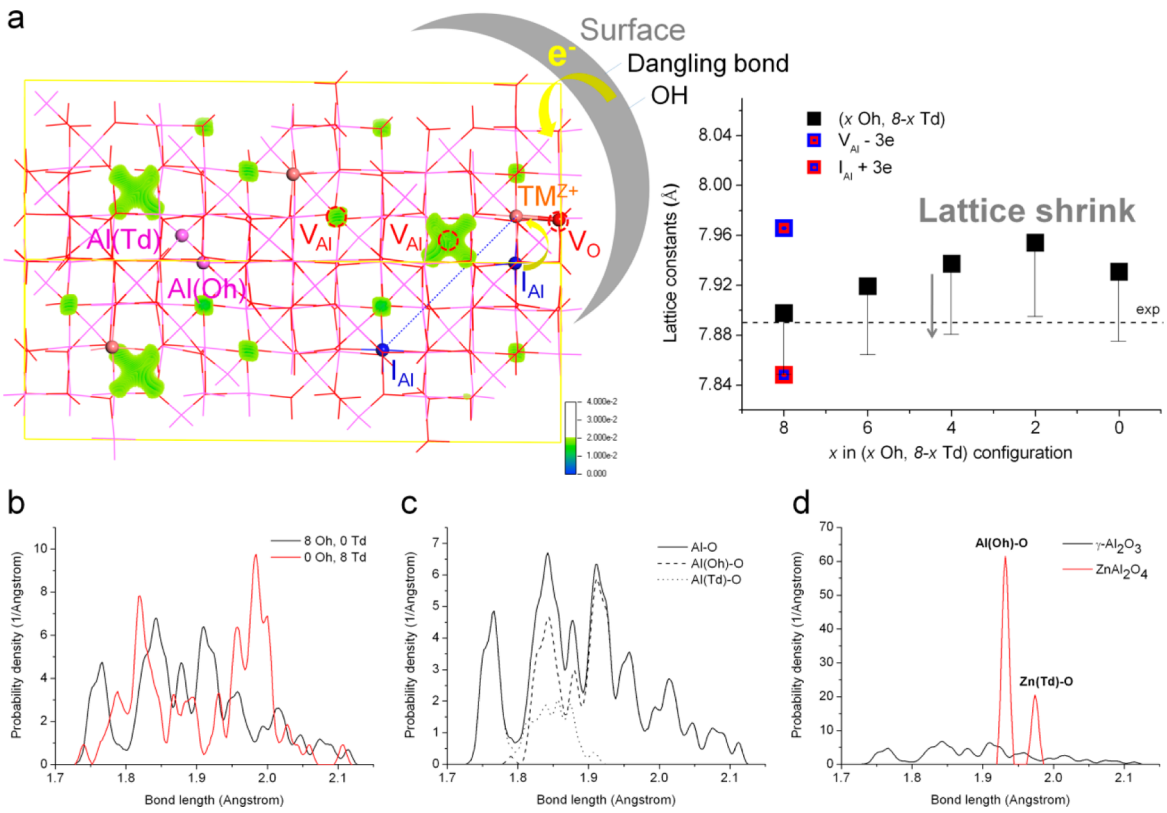

Figure 3. (a) The structure of γ-Al_2O_3 and the lattice constants variation under (x Oh, $8 - x$ Td) configurations with charge compensated I_{Al} or V_{Al}. The Al(Oh)/Al(Td) sites (purple), TM^{Z+} dopants (brown), and intrinsic defects I_{Al} (blue), and $V_{Al(Oh)}$, $V_{Al(Td)}$, and V_O (red) are highlighted. Electron density around V_{Al} sites is given, with the contour line ending at 0.02 e/Å^3. An overestimate of lattice constants by 1.01 is corrected by comparing cal/exp (4.805 Å/4.759 Å) results of corundum (rhombohedral cell). (b) Bond length distribution of γ-Al_2O_3 with (8 Oh, 0 Td) or (0 Oh, 8 Td) configuration. (c) Bond length distribution of (8 Oh, 0 Td) γ-Al_2O_3 and the corresponding Al(Oh)−O and Al(Td)−O bonds. (d) Bond length distribution of (8 Oh, 0 Td) γ-Al_2O_3 and $ZnAl_2O_4$.

the spinel model gives the best fit to bulk features[34] (broadened peaks attributed to lattice distortion), the spinel structure of γ-Al_2O_3[69] with the space group *Fd3* is adopted for DFT calculations (Figure 3a). In order to satisfy the stoichiometry, 8 Al vacancies (V_{Al}) are needed for a 3 × 1 × 1 supercell. The charge compensation is achieved by introducing an intrinsic defect, i.e., an V_{Al} at Oh site, or interstitially adding an extra Al atom (I_{Al}, these I_{Al} which are indistinguishable from normal Al on cation sites can be called pseudointerstitial Al atoms) into the V_{Al} site of the defective spinel lattice, to maintain the electrical neutrality. (x Oh, $8 - x$ Td) configuration represents that there are x V_{Al} at Oh site ($V_{Al(Oh)}$) and $8 - x$ V_{Al} at Td site ($V_{Al(Td)}$) of γ-Al_2O_3. (x Oh, $8 - x$ Td + V_{Al}) or (x Oh, $8 - x$ Td + I_{Al}) configuration represents introducing one V_{Al} or I_{Al} at the Oh site of γ-Al_2O_3.

While different distributions of aluminum ions and vacancies over octahedral and tetrahedral sites have been observed in different γ-Al_2O_3 samples,[34,70−72] DFT studies found that the formation energy of Al vacancies at Oh sites is slightly higher than for Td sites,[73−76] increased by 0.1 eV (per Al_2O_3 unit) for Al(Oh) occupation from 62.5% to 72% (x from 8 to 2).[34] This calculated energy difference is small enough to be consistent with variations in distribution seen in synthetic samples, particularly since configurational entropy also plays a role, favoring more disorder (Table S2). After correcting the overestimate of PBE functional for Al−O using corundum as a reference, the difference between experimental and calculated lattice parameter of γ-Al_2O_3 is less than 0.008 Å, which is close to experimental error. There are some major changes in the nano γ-Al_2O_3 structure, increase of the surface area, change of the surface groups (dangling bonds, hydroxylation), increase of Oh/Td ratio, and formation of extra defects which are charge balanced by surface groups. Hence, some metastable configurations with V_{Al} occupying Td sites, which have slightly higher formation enthalpies, can be stabilized in nanoparticles,[34] and the lattice constants will shrink due to the charge balance from surface groups.

The major difference in the calculated Al−O bond distribution configurations is that a higher Al(Oh) vacancy concentration leads to a longer Al−O bond length (Figure 3b), since the majority of Al−O bond lengths over 1.90 Å are contributed by Al(Oh)−O (Figure 3c). The most important factor contributing to the different cation distribution associated with TM doping in γ-Al_2O_3 and other alumina-based spinel oxides is the variable and highly disperse Al−O bond length distribution. The optimized Al−O bond lengths range from approximately 1.7 to 2.2 Å, reflecting more variable bonding due to disorder and cation vacancies. Illustrating these differences, there is only a very narrow distribution of Al(Oh)−O bond lengths in $ZnAl_2O_4$ (a normal spinel with no tetrahedral aluminum or octahedral zinc) compared to γ-Al_2O_3 (Figure 3d).

Electronic Structure. The electronic structure changes upon metal doping are complicated due to several potential competing factors: (1) the variation of the oxidation state Z of TM^{Z+} dopants and the spin state of the TM, (2) the cation

DOI: 10.1021/acs.chemmater.6b05041
Chem. Mater. 2017, 29, 1338−1349

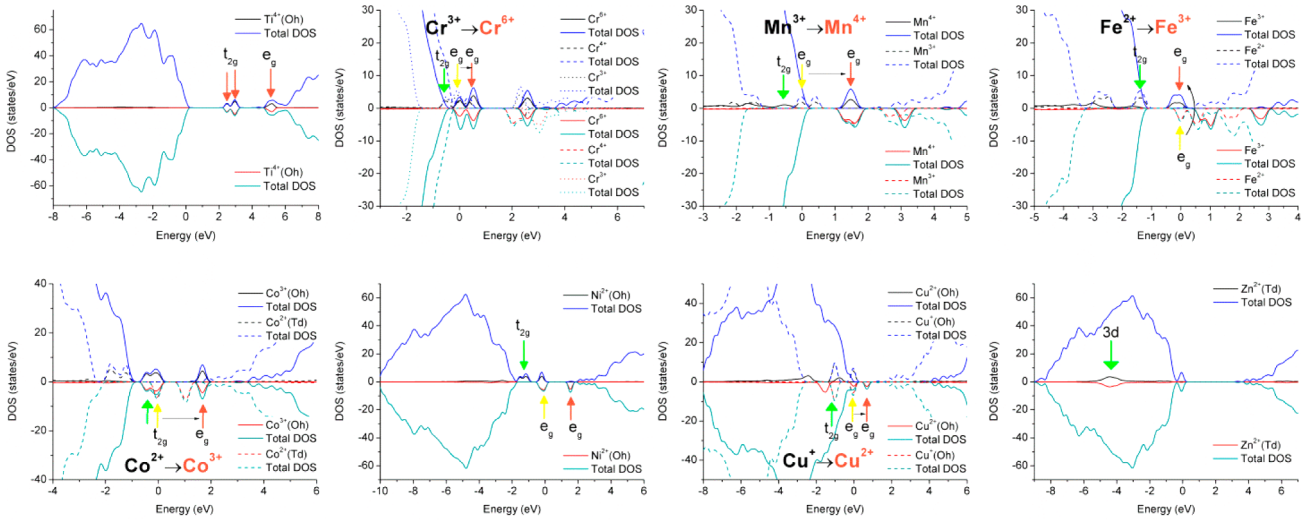

Figure 4. Total density of states (DOS) and atom-projected density of states (PDOS) of the most stable configurations for each TM doped γ-Al_2O_3 are given. The electron transfer from the highest occupied orbital of TM^{Z+} to the lowest unoccupied orbital of $TM^{(Z+\delta)+}$ is given, and the 3d orbitals are shown by colored arrows.

distribution of TM^{Z+} at Oh and Td sites, where the interaction between cations is distance dependent due to coulomb screening effects, and (3) the vacancy content governed by TM doping and resulting charge balance and stoichiometry constraints. Two schemes of charge compensation are considered: In one case, an Al^{3+} ion is replaced by TM^{Z+} ion and the charge balance is achieved by adding $n = Z - 3$ charge to the background system, forming (x TM(Oh) + V_{Al}^S) or (x TM(Oh) + I_{Al}^S) configuration with charge compensation by V_{Al} or I_{Al} at the surface (Table S3). In the other case, three Al^{3+} ions are replaced by TM^{Z+} ions; one V_{Al} is added to compensate three TM^{4+} dopants, or one I_{Al} is added to compensate three TM^{2+} dopants in the system, forming (3 TM^{4+}(Oh) + V_{Al}) or (3 TM^{2+}(Oh) + I_{Al}) configuration (Table S4). DFT calculations (Figure S6) for $Ti^{3+}(d^1)$, $V^{3+}(d^2)$, $Cr^{3+}(d^3)$, $Mn^{3+}(d^4)$, $Fe^{3+}(d^5)$, $Co^{3+}(d^6)$, $Ni^{3+}(d^7)$, $Cu^{3+}(d^8)$, and $Zn^{3+}(d^9)$ in Oh or Td symmetry imply that the split energy levels are influenced by the spin polarization configurations, especially for Fe and Co. The orbital splitting between e_g orbitals and t_{2g} orbitals under HS configurations are much stronger than LS configurations. Except for Ti and Zn, the d−d transition of TM^{Z+}(Td) species is always from e_g orbitals to the t_{2g} orbital, while that of TM^{Z+}(Oh) species is from the occupied t_{2g} orbitals (dxy, dyz, and dzx) to unoccupied e_g orbital (d_{x2-y2} or d_{z2}, depending on its local structural distortion). The PDOS for the predominant species in TM doped γ-Al_2O_3 structures, TM^{4+} (Ti^{4+}(Oh), $Cr^{3+\delta}$(Oh), and $Mn^{3+\delta}$(Oh)), TM^{3+} (Cr^{3+}(Oh), Mn^{3+}(Oh), and Fe^{3+}(Oh)), or TM^{2+} (Co^{2+}(Td), Ni^{2+}(Oh), Cu^{2+}(Oh), and Zn^{2+}(Td)), are shown in Figure 4.

Losing electrons to intrinsic defects V_{Al} seem to change $Ti^{3+}(d^1)$ species to $Ti^{4+}(d^0)$ species, $Cr^{3+}(d^3)$ species to $Cr^{6+}(d^0)$ species, and $Mn^{3+}(d^4)$ species to $Mn^{4+}(d^3)$ species. The transfer of electrons from $Ti^{3+}(d^1)$ species to V_{Al} will compensate the acceptor type dopant of V_{Al}, leading to the formation of $Ti^{4+}(d^0)$, and make the electronic structure similar to TiO_2. In the same way, the $Cr^{6+}(d^0)$ doping will make alumina more like CrO_3 though the orbital splitting of Cr^{6+}(Oh) is larger than that in CrO_3. The orbital splitting between e_g orbitals and t_{2g} orbitals of $Mn^{4+}(d^3)$ and $Ni^{2+}(d^8)$ in spinel alumina is similar to that in ZnO or TiO_2,[14,77] while that of $Fe^{3+}(d^5)$, $Co^{2+}(d^6)$, and $Zn^{2+}(d^{10})$ is much larger than in their own oxides. The occupation of the highest e_g orbital by the electrons from I_{Al} will lead to $Cu^+(d^{10})$ species with fully occupied d orbitals. It is observed that gaining electrons from intrinsic defects, such as I_{Al}, seems to reduce the orbital splitting between occupied t_{2g} orbitals and the highest unoccupied e_g orbital since the excess electron will occupy the highest e_g (t_{2g} for Co and Zn dopant) orbital. Losing electrons, in contrast, will enhance the orbital splitting. The charge density analysis shows that the extra d electrons for TM are almost totally located within the muffin-tin sphere of the substituted site.

The conduction band maximum (CBM) and valence band maximum (VBM) of TM-doped γ-Al_2O_3 are lowered or raised from those of pure γ-Al_2O_3, depending not only on the doping site (Oh or Td) but also on the chemical state and spin state of the dopants. Specifically, Ti, V, Cr, Mn, or Fe doping introduces several 3d states below CBM, while Mn, Fe, Co, Ni, and Cu doping introduces 3d states in the middle of the gap (minor contribution is made to the valence band). Zn doping introduces d orbitals that overlap within the valence band (7−9 eV). For Cu doping, the outermost electron states at the upper part (0 to 2 eV) of the valence band are mainly contributed by Cu^+ species while the lower part (2 to 4 eV) is by the Cu^{2+} species. Similarly, Cr or Ni doping also increases the width of the valence band by introducing 3d states that mix with O 2p states above VBM and extends the valence band edge.

On the basis of the above discussions, the excitation peaks in XPS valence band spectra (Figure 5) can be assigned and the influence of TM doping on the band edge of γ-Al_2O_3 is clarified. The charge compensation from I_{Al} or V_{Al} leads to the upward or downward shift of the Fermi level. While Cu, Ni, and Cr dopants introduce band tails near the Fermi level (2−4 eV), Zn introduces some deep valence states (10−12 eV).

Dopant Site Preference in Bulk and Nano γ-Al_2O_3. For the bulk TM-doped γ-Al_2O_3, we estimated the substitution cost using the approach described earlier (for details, see the Supporting Information).[34] Figure 6a presents the site preference energies ($E_{\text{site preference}}$), i.e., the calculated formation energy difference between TM^{Z+} (Z = 2, 3, 4) doping at the Al(Oh) and Al(Td) sites of bulk γ-Al_2O_3. No significant correlation between energy and volume change is found (Table S3).

DOI: 10.1021/acs.chemmater.6b05041
Chem. Mater. 2017, 29, 1338−1349

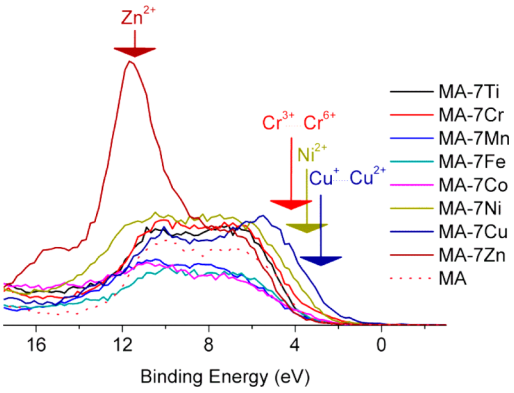

Figure 5. Valence band XPS spectra of MA-7TM samples.

At low doping level, while all TM^{4+} prefers the Oh site (red diamond), the site preferences for TM^{3+} (pink) and TM^{2+} (blue) are more complicated, which is influenced by two factors under the nano effect: the lattice distortion (shadow region) and the increase of Oh/Td ratio in the γ-Al_2O_3 (sphere). Due to the defect nature of γ-Al_2O_3, the local bonding environments are disturbed randomly, and the distorted Oh/Td symmetry will lead to the variation of lattice energy of about 0.2 eV from site to site (see error bar for Cu). Moreover, the site preference of the dopant may also be impacted by nano effects. We employed the (2 Td, 6 Oh) configuration as a model to investigate the E_{subs} of TM doping for nanosized γ-Al_2O_3. While the lattice energy decreased by up to 0.04 eV (per Al_2O_3 unit) due to the 1% volume expansion under this nano effect, a similar trend of dopant site preference was observed as for bulk material but with Oh site preference energy lowered by 0−0.2 eV (Figure 6a). Cr^{3+} and Co^{3+} strongly prefer the Oh site, while Ti^{3+}, V^{3+}, Mn^{3+}, Ni^{3+}, Ni^{2+}, and Cu^{3+} weakly prefer it. The strong preference of Fe^{2+}, Co^{2+}, Ni^{2+}, Cu^{2+}, and Zn^{2+} for the Td site (blue diamond) is weakened after the increase of Oh/Td ratio in γ-Al_2O_3 (blue sphere). Under the nano effect, these dopants will be statistically distributed at Oh or Td sites in the γ-Al_2O_3 structure (randomly distributed), except for Co^{2+} and Zn^{2+}, which still have strong preferences for the Td site. This observation is in good agreement with the well-known trends that atoms with shallow valence d states tend to occupy the Td site rather than the Oh site and that ions with d^{10} configurations, like Zn^{2+} and Cd^{2+}, prefer tetrahedral coordination.[78] Although the general cation distribution rules for simple spinels do not fully apply in this case, similar site preference of Cr^{3+}, Mn^{3+}, Ni^{2+}, and Cu^{2+} at Oh site and Zn^{2+} at Td site were obtained using simple models with Al^{3+} as a reference ion.[42−44] Furthermore, to explore the supercell size effect, we also studied the TM doping preference in a $3 \times \sqrt{2} \times \sqrt{2}$ supercell and the observed trend remains (not shown). It should be mentioned that the present work cannot exclude the

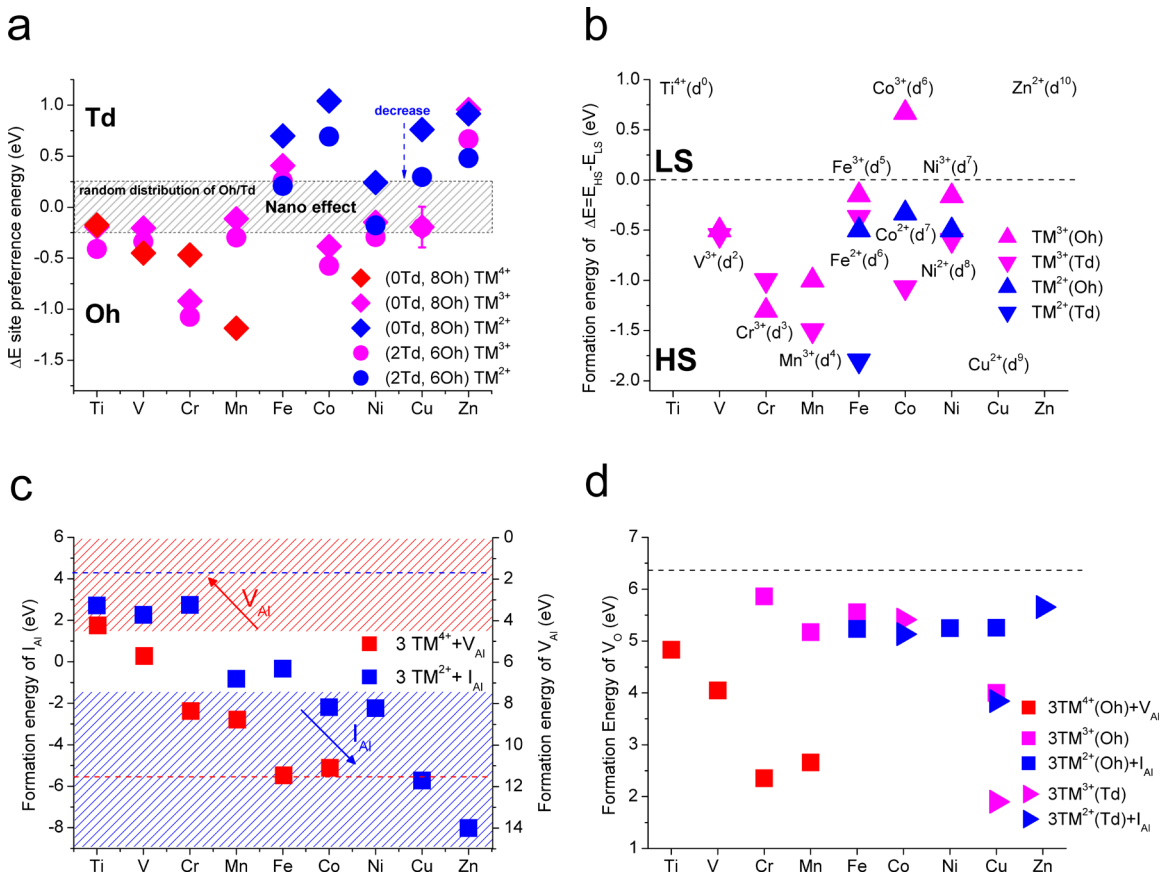

Figure 6. Preferred doping site, spin state, and the formation energy of intrinsic defects upon TM doping. (a) The $E_{site\ preference}$ for TM^{Z+} (Z = 2, 3, 4) in γ-Al_2O_3 with (0 Td, 8 Oh) or (2 Td, 6 Oh) configuration. Error bars represent results from 12 nonequivalent sites. (b) The formation energy difference between HS and LS configurations. (c) The formation energy of V_{Al} in ($3TM^{4+}$) configurations or I_{Al} in ($3TM^{2+}$) configurations, and the corresponding formation energy of I_{Al} (blue line) or V_{Al} (red line) in pure γ-Al_2O_3. (d) The formation energy of V_O and the corresponding formation energy of V_O (black line) in pure γ-Al_2O_3.

DOI: 10.1021/acs.chemmater.6b05041
Chem. Mater. 2017, 29, 1338−1349

change of site preference energies at high doping levels, as reported previously.[34]

Spin State Preference. The formation energy differences between the highest spin (HS) and lowest spin (LS) configurations for each type of TM atom in γ-Al_2O_3, at Al(Oh) or Al(Td) site, are listed in Figure 6b. Not seen in ZnO or TiO_2,[14,77] the spin configurations in γ-Al_2O_3 can be categorized into three types: (1) For TM dopants with completely filled d orbitals, such as $Ti^{4+}(d^0)$ and $Zn^{2+}(d^{10})$, there are no other spin configurations observed. (2) For TM dopants with partially filled d orbitals, such as $V^{3+}(d^2)$, $Cr^{3+}(d^3)$, $Mn^{3+}(d^4)$, $Fe^{3+}(d^5)$, $Fe^{2+}(d^6)$, $Co^{2+}(d^7)$, and $Ni^{2+}(d^8)$, the formations of high spin configurations are much more favorable, except $Co^{3+}(d^6)$, which favor the nonmagnetic configuration where all six t_{2g} orbitals are filled. (3) The high spin paramagnetic $Cu^{2+}(d^9)$ with only one unfilled 3d orbital.

Charge Compensation by Intrinsic Defects in γ-Al_2O_3. The mechanism of charge compensation by the intrinsic defects in γ-Al_2O_3, including one I_{Al} or V_{Al} in a $3 \times 1 \times 1$ supercell doped by three TM atoms (at the preferred site), was investigated. Overall, the charge compensation for TM dopants by Al can be divided into three regions (Figure 6c). The high formation energies of I_{Al} in Ti, V, and Cr and Mn doped γ-Al_2O_3 (red region) indicate that, even when dopant cation charge can be equal to or larger than 3, the formation of V_{Al} in the bulk structure is still unlikely. In contrast, the low formation energies of I_{Al} upon doping of Co, Ni, Cu, and Zn (green region) suggest that I_{Al} is favored once a TM^{Z+} with a charge smaller than 3 is introduced. For Cr, Mn, and Fe (in the middle regions), the formation of either V_{Al} or I_{Al} is energetically unfavored. Generally, our DFT calculation suggests that the Al content in γ-Al_2O_3 tends to increase as the atomic number of TM increases. The binding energies of TM appear to vary in a complicated manner due to the correlated effect from TM dopants and V_{Al} of γ-Al_2O_3.

Although the formation energy of V_{Al} in the bulk structure for Ti, Cr, and Mn doping is high (Figure 6c), if we consider the observed lowered defect formation energy in other oxides, we can reasonably suggest the formation of V_{Al} for Ti doping. On the basis of DFT calculations and ionic size considerations, Cr^{6+} and Cr^{4+} are probably only on the surface. The calculations were repeated for a few equivalent sites, and the differences were minor. Some representative structures are listed (Figure S7). It is observed that under Jahn−Teller effect the TM−O bonds are shortened or elongated, and the deformation around the Oh/Td structure varies randomly.

Valence States. Valence identification of TM dopants in γ-Al_2O_3 is challenging. It is well observed that normally the binding energy of TM^{Z+} in metal aluminate spinel is higher than that in its corresponding transition metal oxide.[61] Such energetic difference will introduce additional complexity for identifying the valence state of TM in γ-Al_2O_3. Specifically, the TM^{2+} and TM^{3+} species are not readily distinguished in this case. Combining DFT calculation and 2p3/2 XPS, we analyzed the Mulliken charge and oxidation states of each TM dopant in γ-Al_2O_3 (Table 1), by comparing our results with the previously reported 2p XPS data of TM oxides (Figure S4).[61] The binding energy of TM^{2+}, which is in line with Mulliken charge, is increased by two factors. For TM^{Z+} with the same valence state, $TMAl_2O_4$ gives a higher binding energy over simple transition metal oxides (TMO) while the dispersed TM^{Z+} species gives higher binding energy than aggregated species.

The inferred binding energy and oxidation state of each TM are then derived and summarized in Table 1. For clarity, the predominant species of TM are listed in bold. For example, the calculated Mulliken charge for Fe^{3+}(Oh)/Fe^{2+}(Oh) and Fe^{3+}(Oh)/Fe^{3+}(Td) are 1.20/0.96 and 1.20/1.13, respectively. Hence, for the MA-7Fe sample, the Fe 2p3/2 binding energies at 712.3 and 711.3 eV are attributed to Fe^{3+} and Fe^{2+}, respectively. Similarly, for MA-7Co, the Co 2p3/2 signals at 781.7 and 782.1 eV are assigned to Co^{2+}(Td) and Co^{2+}(Oh), respectively. The valence states of TM dopant in γ-Al_2O_3 are related to the formation enthalpies of the corresponding TM oxides and γ-Al_2O_3 (Table S5).[79] The Ti doped in γ-Al_2O_3 maintains a high oxidation state (+4) due to the higher formation enthalpy of TiO_2 compared to that of γ-Al_2O_3. In contrast, the oxidation states of other TM dopant atoms tend to approach +3, appearing to be governed by the surrounding γ-Al_2O_3 reservoir due to the lower lattice energy of other TM oxides than that of γ-Al_2O_3. Correspondingly, due to the charge compensation effect, TM^{Z+} dopants with oxidation state Z larger than 3 will induce more Al deficiency, while for TM dopants with Z lower than +3, I_{Al} is introduced and the corresponding formation energy of I_{Al} increases with the increased atomic number of TM. It should be mentioned that such charge compensation effect is distance dependent.

On the other hand, TM doping in γ-Al_2O_3 also significantly lowers the formation energy of V_O (Figure 6d, pink), due to the weak covalent TM−O bond (similar to the case in the corresponding TM oxide) compared with the strong Al−O bond. Considering the charge compensation of V_{Al} (red) or I_{Al} (blue), the formation energy of V_O under TM doping is significantly reduced. The formation energy is also strongly influenced by local symmetry around TM, as found for Cu, in which the formation energy of V_O at Td site is lowered by 1.5 eV compared to that at the Oh site.

Optical Properties. From the electronic structure, optical properties of TM doped γ-Al_2O_3 have been calculated in order to interpret the UV−vis spectra for MA-7TM samples (Figure 2b). While Ti doping induces a large red-shift of the absorption edge, Cr, Mn, Fe, and Co doping all induce distinctive visible light absorption bands. These visible absorption bands are determined by the separation between e_g and t_{2g} states, i.e., the weakly allowed d−d transition of the TM ions. The absorption edge is slightly changed by Co or Zn doping. While both $Co^{2+}(d^7)$ and $Ni^{2+}(d^8)$ introduce a strong absorption band around 600 nm, both $Cr^{3+}(d^3)$ and $Cu^{2+}(d^9)$ only introduce a medium absorption band around 600 nm. In contrast, dopants with half-filled or filled d orbitals such as $Fe^{3+}(d^5)$, $Cr^{6+}(d^0)$, and $Cu^{+}(d^{10})$ all introduce a strong band around 400 nm due to the LM (ligand to metal) excitation. The situation for Mn doping is between the above two types of excitation mechanisms due to the mixed oxidation states ($Mn^{4+}(d^3)$ and $Mn^{3+}(d^4)$). Due to the large orbital splitting of $Mn^{3+}(d^4)$ orbitals, the absorption edge is due to the excitation from O 2p to Mn 3d orbitals.

Lattice Parameter Variation. The influence of TM doping on the lattice parameter of γ-Al_2O_3 is shown in Figure S8. The lattice parameter change under charge compensation by I_{Al} on the surface (diamond) is significantly larger than that caused by I_{Al} in the bulk structure (square), and lattice shrinkage occurs only when V_{Al}^S is introduced while significant lattice expansion occurs only when I_{Al}^s is formed.

Overall Trends and Implications. The one-pot procedure produces mesoporous structure after the self-assembly process

DOI: 10.1021/acs.chemmater.6b05041
Chem. Mater. 2017, 29, 1338−1349

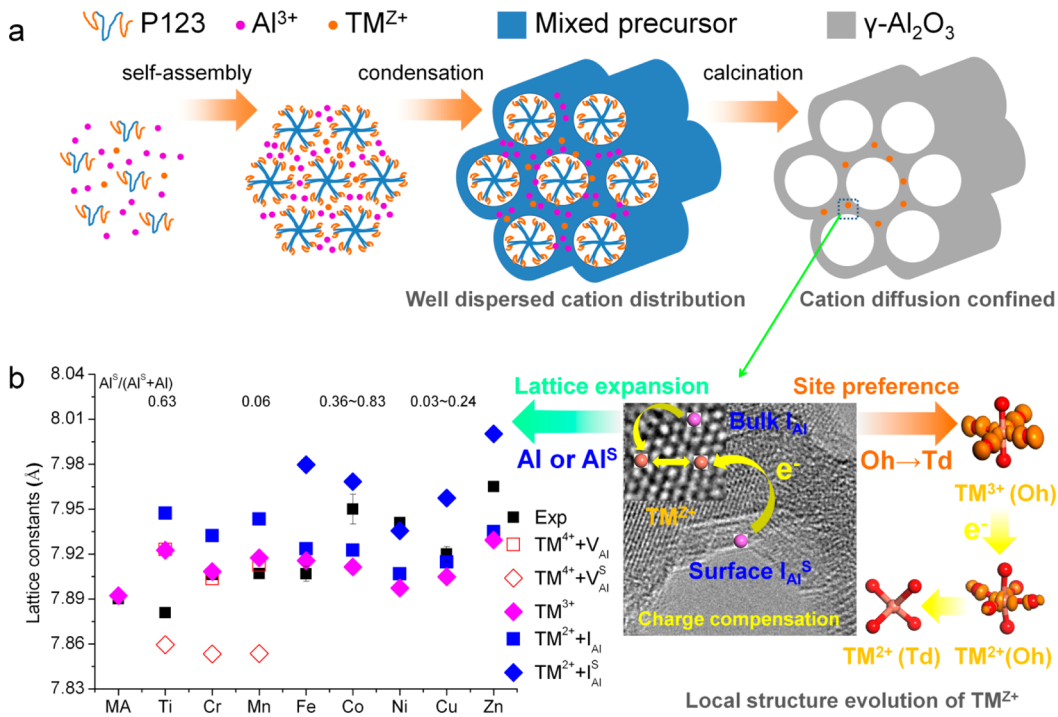

Figure 7. (a) The doping mechanism of TM^{Z+} in MA-7TM. (b) The lattice constants from XRD experimental (black) and DFT calculations for TM^{Z+} doped γ-Al_2O_3 with $Z = 4$ (red), 3 (pink), or 2 (blue). The lattice expansion by TM^{Z+} doping under charge compensation by V_{Al}/I_{Al} in bulk structure (square) or V_{Al}^S/I_{Al}^S on the surface (diamond) is given. The estimated ratios of $Al^S/(Al^S + Al)$ are given. The consequent local structure evolution of TM^{Z+} with the decrease of valence state under charge compensation is demonstrated, i.e., the site preference change from Oh to Td.

with the help of surfactant P_{123}, while the metal dopants are well dispersed in precursor framework during the condensation process (Figure 7a). Although the mesostructure of mesoporous γ-Al_2O_3 is composed of nano γ-Al_2O_3 particles with higher surface area, the actual atomic configurations are not only driven by the energy-minimizing mechanisms (moving toward equilibrium) but also depend on the detailed preparation conditions (representing some kinetic constraints). While the mixed metal precursors are heat-treated with the presence of TM^{Z+} ions, the transformation to cubic spinel will take place with bond breaking where Al^{3+} or TM^{Z+} ions would be well dispersed and occupy Oh or Td sites, depending on their own lattice stability and also highly influenced by charge compensation.

As shown in Figure 4, the spin state, the orbital coupling under various local structures (Oh or Td), nano effect, and the charge compensation effect are the key factors for the doping mechanism of TM in γ-alumina. While formation of intrinsic defects in nanoparticles can be greatly enhanced, the chemical state of the well dispersed TM dopant in γ-Al_2O_3 varies accordingly, by gaining electrons from I_{Al} or losing electrons to V_{Al} defects or surface hydroxyl groups under the coulomb screening effect. As is well-known, the local structure and magnetic behavior of TM-doped oxides are strongly sensitive to the preparation parameters, such as oxygen partial pressure, temperature, doping element, and level.[18]

Generally, impregnation methods give disperse metal catalysts on the alumina surface, while one-pot synthesis gives dispersed metal dopants in the alumina lattice. The homogeneous distribution of metal species in the support structure will alter the thermal stability, isoelectric point, and electronic properties. On the basis of charge compensation (Figure 4c), the variation of charge state of dopants can be rationalized. From a crystallization point of view, the decrease of Al vacancy concentration appears to favor the growth of spinels with higher crystallinity and bigger grain size. The high concentration of V_{Al} introduced by Ti doping seems to hinder the formation of a spinel with high crystallinity while, on the contrary, Zn doping accelerates the crystallization process, as shown by the WXRD results (Figure S9 and Table S1). Besides, taking into account the lattice parameters (Tables S3 and S4) and TM concentrations (Table S1), the influence of lattice expansion for MA-7TM samples can be rationalized. As shown (Figure 7b), the amounts of defects at the surface, V_{Al}^S or I_{Al}^S, in each sample are deduced accordingly, which indicates that the distribution of Al defects at bulk (Al) or surface (Al^S) varies from case to case, and the lattice parameters are highly influenced by the detailed synthesis conditions. While some slightly distorted structures show diamagnetic properties, the slight elongation of several TM−O bonds at one side of the Oh or Td structure makes them paramagnetic and lowers the total enthalpy. The $TM^{(z\pm\delta)+}$ species, being low-valence dopants or high-valence dopants,[13] can be further reduced or oxidized, with their TM−O bonds and structures varied accordingly. The excess or loss of electrons would lengthen or shorten the TM−O bond slightly (0−0.2 Å) and lead to the site preference shift from Oh to Td.

Codoping is sometimes found to be beneficial for catalytic reactions.[80] As an example, for Cr + Zn codoping in MA, while Cr and Zn are homogeneously distributed in mesoporous alumina, the Cr doping enhances the formation of V_{Al}; as a result, the lattice parameter is decreased (Figure S10) and Cr^{6+} species, which is mainly on the surface, is greatly decreased (Figure 8).

The orbital coupling between nearby TM atoms will increase with the TM concentrations due to the increased electron

DOI: 10.1021/acs.chemmater.6b05041
Chem. Mater. 2017, 29, 1338−1349

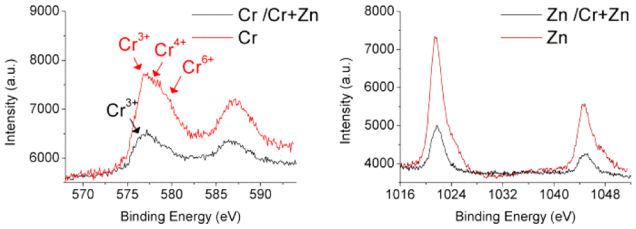

Figure 8. Cr 2p and Zn 2p XPS spectra of MA-7Cr, MA-7Zn, and MA-7(Cr + Zn).

correlations. While there are some red-shifts of the absorption edge, the absorption band in the visible light range is mainly due to the d−d transition of the dispersed TM^{Z+}(Oh/Td) species, which also has been shifted by the electrons from or to these coexisting intrinsic defects. Hence, the visible light absorption abilities, as well as the transfer ability of excited photoelectron, which is crucial for photoreactions, can be improved in such a way. It is expected that the further design of such kind of a metal doped mesoporous alumina support can be elucidated by our DFT calculations.

■ CONCLUSIONS

The cooperative effect of TM dopants and intrinsic defects (cation vacancies) upon γ-Al_2O_3 is studied by first-principles calculations, and a series of ordered mesoporous alumina tailored by TM dopants is synthesized and characterized. The cation distribution and the energetically favorable structures are clarified and compared with the experimental findings from TM-doped Al_2O_3. While the TM dopants are well dispersed in the alumina lattice via the one-pot routine, the real atomic configurations are complicated. The analysis of electronic structure combining the experimental characterization and DFT calculations indicates that the charge compensation effect, nano effect, and the orbital splitting under different cation distribution (Oh or Td, well dispersed or aggregated, bulk or surface) are the key factors for the doping mechanism. As a result, the Al content in γ-Al_2O_3 increases with the atomic number of the TM dopants, while O content only decreases around TM−O regions. Furthermore, the optical properties of Al_2O_3 have been tuned by the well dispersed TM dopants that coexisted with the intrinsic defects (I_{Al}/V_{Al}). While there are some degrees of red-shift of the absorption edge, the absorption band in the visible light range are mainly due to the d−d transition of TM^{Z+}(Oh/Td) species, slightly shifted by the electrons from or to these coexisting intrinsic defects. The mesoporous alumina, with defect spinel alumina structures, possesses a distinctive doping mechanism from other oxides, and the change of V_{Al} concentration under metal doping will greatly alter the intrinsic property of alumina. On the basis of the above understanding, the future tailoring of alumina support by metal dopants might be guided by this work.

■ ASSOCIATED CONTENT

Supporting Information

The Supporting Information is available free of charge on the ACS Publications website at DOI: 10.1021/acs.chemmater.6b05041.

Details of surface area, crystal size, lattice constants, and TM concentration of MA-7TM samples; XRD, BET, and XPS measurement of MA-7TM samples; the calculated total energy, charge, average lattice constant, density of states, and local structures of TM^{Z+}-doped γ-Al_2O_3 (PDF)

■ AUTHOR INFORMATION

Corresponding Authors

*E-mail: hmyang@csu.edu.cn.
*E-mail: d.wu@wsu.edu.
*E-mail: anavrotsky@ucdavis.edu.

ORCID

Liangjie Fu: 0000-0002-9761-5305
Di Wu: 0000-0001-6879-321X
Alexandra Navrotsky: 0000-0002-3260-0364

Notes

The authors declare no competing financial interest.

■ ACKNOWLEDGMENTS

This work was supported by the National Science Fund for Distinguished Young Scholars (51225403), the Hunan Provincial Science and Technology Project (2016RS2004), and the Postdoctoral Science Foundation of Central South University (201507). All computations were performed at the High Performance Computing Center of Central South University. D.W. thanks the institutional funds from the Gene and Linda Voiland School of Chemical Engineering and Bioengineering at Washington State University.

■ REFERENCES

(1) McHale, J. M.; Auroux, A.; Perrotta, A. J.; Navrotsky, A. Surface Energies and Thermodynamic Phase Stability in Nanocrystalline Aluminas. *Science* **1997**, *277*, 788−791.

(2) Barakat, T.; Rooke, J. C.; Genty, E.; Cousin, R.; Siffert, S.; Su, B.-L. Gold Catalysts in Environmental Remediation and Water-Gas Shift Technologies. *Energy Environ. Sci.* **2013**, *6*, 371−391.

(3) Kwak, J. H.; Hu, J.; Mei, D.; Yi, C.-W.; Kim, D. H.; Peden, C. H. F.; Allard, L. F.; Szanyi, J. Coordinatively Unsaturated Al^{3+} Centers as Binding Sites for Active Catalyst Phases of Platinum on Gamma-Al_2O_3. *Science* **2009**, *325*, 1670−1673.

(4) Do, P. T. M.; Foster, A. J.; Chen, J.; Lobo, R. F. Bimetallic Effects in the Hydrodeoxygenation of Meta-Cresol on γ-Al_2O_3 Supported Pt−Ni and Pt−Co Catalysts. *Green Chem.* **2012**, *14*, 1388−1397.

(5) Bagshaw, S. A.; Prouzet, E.; Pinnavaia, T. J. Templating of Mesoporous Molecular Sieves by Nonionic Polyethylene Oxide Surfactants. *Science* **1995**, *269*, 1242−1244.

(6) Huo, Q.; Margolese, D. I.; Ciesla, U.; Demuth, D. G.; Feng, P.; Gier, T. E.; Sieger, P.; Firouzi, A.; Chmelka, B. F.; Schüth, F.; Stucky, G. D. Organization of Organic Molecules with Inorganic Molecular Species into Nanocomposite Biphase Arrays. *Chem. Mater.* **1994**, *6*, 1176−1191.

(7) Bagshaw, S. A.; Pinnavaia, T. J. Mesoporous Alumina Molecular Sieves. *Angew. Chem., Int. Ed. Engl.* **1996**, *35*, 1102−1105.

(8) Vaudry, F.; Khodabandeh, S.; Davis, M. E. Synthesis of Pure Alumina Mesoporous Materials. *Chem. Mater.* **1996**, *8*, 1451−1464.

(9) Čejka, J. Organized Mesoporous Alumina: Synthesis, Structure and Potential in Catalysis. *Appl. Catal., A* **2003**, *254*, 327−338.

(10) Márquez-Alvarez, C.; Žilková, N.; Pérez-Pariente, J.; Čejka, J. Synthesis, Characterization and Catalytic Applications of Organized Mesoporous Aluminas. *Catal. Rev.: Sci. Eng.* **2008**, *50*, 222−286.

(11) Trueba, M.; Trasatti, S. P. γ-Alumina as a Support for Catalysts: A Review of Fundamental Aspects. *Eur. J. Inorg. Chem.* **2005**, *2005*, 3393−3403.

(12) Lee, S.; Molina, L. M.; López, M. J.; Alonso, J. a; Hammer, B.; Lee, B.; Seifert, S.; Winans, R. E.; Elam, J. W.; Pellin, M. J.; Vajda, S. Selective Propene Epoxidation on Immobilized Au_{6-10} Clusters: The Effect of Hydrogen and Water on Activity and Selectivity. *Angew. Chem., Int. Ed.* **2009**, *48*, 1467−1471.

DOI: 10.1021/acs.chemmater.6b05041
Chem. Mater. 2017, 29, 1338−1349

(13) McFarland, E. W.; Metiu, H. Catalysis by Doped Oxides. *Chem. Rev.* **2013**, *113*, 4391−4427.
(14) Janisch, R.; Gopal, P.; Spaldin, N. A. Transition Metal-Doped TiO_2 and ZnO—present Status of the Field. *J. Phys.: Condens. Matter* **2005**, *17*, R657−R689.
(15) Umebayashi, T.; Yamaki, T.; Itoh, H.; Asai, K. Analysis of Electronic Structures of 3d Transition Metal-Doped TiO_2 Based on Band Calculations. *J. Phys. Chem. Solids* **2002**, *63*, 1909−1920.
(16) Matsumoto, Y.; Murakami, M.; Shono, T.; Hasegawa, T.; Fukumura, T.; Kawasaki, M.; Ahmet, P.; Chikyow, T.; Koshihara, S.; Koinuma, H. Room-Temperature Ferromagnetism in Transparent Transition Metal-Doped Titanium Dioxide. *Science* **2001**, *291*, 854−856.
(17) Wang, Q.; Sun, Q.; Jena, P.; Kawazoe, Y. Magnetic Properties of Transition-Metal-Doped $Zn_{1-x}T_xO$ (T = Cr, Mn, Fe, Co, and Ni) Thin Films with and without Intrinsic Defects: A Density Functional Study. *Phys. Rev. B: Condens. Matter Mater. Phys.* **2009**, *79*, 115407.
(18) Pan, F.; Song, C.; Liu, X. J.; Yang, Y. C.; Zeng, F. Ferromagnetism and Possible Application in Spintronics of Transition-Metal-Doped ZnO Films. *Mater. Sci. Eng., R* **2008**, *62*, 1−35.
(19) Gopal, P.; Spaldin, N. A. Magnetic Interactions in Transition-Metal-Doped ZnO: An Ab Initio Study. *Phys. Rev. B: Condens. Matter Mater. Phys.* **2006**, *74*, 094418.
(20) Chien, C.-H.; Chiou, S. H.; Guo, G. Y.; Yao, Y.-D. Electronic Structure and Magnetic Moments of 3d Transition Metal-Doped ZnO. *J. Magn. Magn. Mater.* **2004**, *282*, 275−278.
(21) Ueda, K.; Tabata, H.; Kawai, T. Magnetic and Electric Properties of Transition-Metal-Doped ZnO Films. *Appl. Phys. Lett.* **2001**, *79*, 988−990.
(22) Lin, C.; Huang, C.; Chen, S.; Zheng, Y.; Shen, P. On the Enhanced Solute Content, Shape, Defect Microstructures, and Optical Properties of Ti-Doped γ-Al_2O_3 Nanocondensates. *J. Phys. Chem. C* **2009**, *113*, 19112−19118.
(23) Weckhuysen, B. M.; Schoonheydt, R. A. Alkane Dehydrogenation over Supported Chromium Oxide Catalysts. *Catal. Today* **1999**, *51*, 223−232.
(24) Sun, L.-B.; Tian, W.-H.; Liu, X.-Q. Magnesia-Incorporated Mesoporous Alumina with Crystalline Frameworks: A Solid Strong Base Derived from Direct Synthesis. *J. Phys. Chem. C* **2009**, *113*, 19172−19178.
(25) Tseng, T.-K.; Chu, H.; Hsu, H.-H. Characterization of γ-Alumina-Supported Manganese Oxide as an Incineration Catalyst for Trichloroethylene. *Environ. Sci. Technol.* **2003**, *37*, 171−176.
(26) Parida, K. M.; Pradhan, A. C. Fe/meso-Al_2O_3: An Efficient Photo-Fenton Catalyst for the Adsorptive Degradation of Phenol. *Ind. Eng. Chem. Res.* **2010**, *49*, 8310−8318.
(27) Shimizu, K.; Maeshima, H.; Satsuma, A.; Hattori, T. Transition Metal-Aluminate Catalysts for NO Reduction by C_3H_6. *Appl. Catal., B* **1998**, *18*, 163−170.
(28) Ji, L.; Lin, J.; Zeng, H. C. Metal−Support Interactions in Co/Al_2O_3 Catalysts: A Comparative Study on Reactivity of Support. *J. Phys. Chem. B* **2000**, *104*, 1783−1790.
(29) Dandapat, A.; De, G. Host-Mediated Synthesis of Cobalt Aluminate/γ-Alumina Nanoflakes: A Dispersible Composite Pigment with High Catalytic Activities. *ACS Appl. Mater. Interfaces* **2012**, *4*, 228−234.
(30) Savva, P. G.; Goundani, K.; Vakros, J.; Bourikas, K.; Fountzoula, C.; Vattis, D.; Lycourghiotis, A.; Kordulis, C. Benzene Hydrogenation over Ni/Al_2O_3 Catalysts Prepared by Conventional and Sol−gel Techniques. *Appl. Catal., B* **2008**, *79*, 199−207.
(31) Águila, G.; Gracia, F.; Cortés, J.; Araya, P. Effect of Copper Species and the Presence of Reaction Products on the Activity of Methane Oxidation on Supported CuO Catalysts. *Appl. Catal., B* **2008**, *77*, 325−338.
(32) Yang, X.; Cao, C.; Klabunde, K. J.; Hohn, K. L.; Erickson, L. E. Adsorptive Desulfurization with Xerogel-Derived Zinc-Based Nanocrystalline Aluminum Oxide. *Ind. Eng. Chem. Res.* **2007**, *46*, 4819−4823.
(33) Yuan, Q.; Yin, A.; Luo, C.; Sun, L.; Zhang, Y.; Duan, W.; Liu, H.; Yan, C. Facile Synthesis for Ordered Mesoporous γ-Aluminas with High Thermal Stability. *J. Am. Chem. Soc.* **2008**, *130*, 3465−3472.
(34) Fu, L.; Yang, H. Tailoring the Electronic Structure of Mesoporous Spinel γ-Al_2O_3 at Atomic Level: Cu-Doped Case. *J. Phys. Chem. C* **2014**, *118*, 14299−14315.
(35) Morris, S. M.; Fulvio, P. F.; Jaroniec, M. Ordered Mesoporous Alumina-Supported Metal Oxides. *J. Am. Chem. Soc.* **2008**, *130*, 15210−15216.
(36) Cai, W.; Yu, J.; Anand, C.; Vinu, A.; Jaroniec, M. Facile Synthesis of Ordered Mesoporous Alumina and Alumina- Supported Metal Oxides with Tailored Adsorption and Framework Properties. *Chem. Mater.* **2011**, *23*, 1147−1157.
(37) Stavale, F.; Shao, X.; Nilius, N.; Freund, H.-J.; Prada, S.; Giordano, L.; Pacchioni, G. Donor Characteristics of Transition-Metal-Doped Oxides: Cr-Doped MgO versus Mo-Doped CaO. *J. Am. Chem. Soc.* **2012**, *134*, 11380−11383.
(38) Xu, L.; Zhao, H.; Song, H.; Chou, L. Ordered Mesoporous Alumina Supported Nickel Based Catalysts for Carbon Dioxide Reforming of Methane. *Int. J. Hydrogen Energy* **2012**, *37*, 7497−7511.
(39) Grant, S. M.; Jaroniec, M. Effect of Acid Concentration on Pore Size in Polymer-Templated Mesoporous Alumina. *J. Mater. Chem.* **2012**, *22*, 86−92.
(40) Sun, L. B.; Yang, J.; Kou, J. H.; Gu, F. N.; Chun, Y.; Wang, Y.; Zhu, J. H.; Zou, Z. G. One-Pot Synthesis of Potassium-Functionalized Mesoporous Gamma-Alumina: A Solid Superbase. *Angew. Chem., Int. Ed.* **2008**, *47*, 3418−3421.
(41) Dunitz, J. D.; Orgel, L. E. Electronic Properties of Transition-Metal Oxides-II:cation Distribution amongst Octahedral and Tetrahedral Sites. *J. Phys. Chem. Solids* **1957**, *3*, 318−323.
(42) Navrotsky, A.; Kleppa, O. J. The Thermodynamics of Cation Distributions in Simple Spinels. *J. Inorg. Nucl. Chem.* **1967**, *29*, 2701−2714.
(43) O'Neill, H. S. C.; Navrotsky, A. Simple Spinels: Crystallographic Parameters, Cation Radii, Lattice Energies, and Cation Distribution. *Am. Mineral.* **1983**, *68*, 181−194.
(44) O'Neill, H. S. C.; Navrotsky, A. Cation Distributions and Thermodynamic Properties of Binary Spinel Solid Solutions. *Am. Mineral.* **1984**, *69*, 733−753.
(45) Stevanović, V.; d'Avezac, M.; Zunger, A. Simple Point-Ion Electrostatic Model Explains the Cation Distribution in Spinel Oxides. *Phys. Rev. Lett.* **2010**, *105*, 075501.
(46) Paudel, T. R.; Zakutayev, A.; Lany, S.; d'Avezac, M.; Zunger, A. Doping Rules and Doping Prototypes in A_2BO_4 Spinel Oxides. *Adv. Funct. Mater.* **2011**, *21*, 4493−4501.
(47) Segall, M.; Lindan, P.; Probert, M. J.; Pickard, C. J.; Hasnip, P. J.; Clark, S. J.; Payne, M. C. First-Principles Simulation: Ideas, Illustrations and the CASTEP Code. *J. Phys.: Condens. Matter* **2002**, *14*, 2717−2744.
(48) Perdew, J. P.; Burke, K.; Ernzerhof, M. Generalized Gradient Approximation Made Simple. *Phys. Rev. Lett.* **1996**, *77*, 3865−3868.
(49) Patra, A. K.; Dutta, A.; Bhaumik, A. Self-Assembled Mesoporous γ-Al_2O_3 Spherical Nanoparticles and Their Efficiency for the Removal of Arsenic from Water. *J. Hazard. Mater.* **2012**, *201−202*, 170−177.
(50) Bilecka, I.; Luo, L.; Djerdj, I.; Rossell, M. D.; Jagodič, M.; Jagličić, Z.; Masubuchi, Y.; Kikkawa, S.; Niederberger, M. Microwave-Assisted Nonaqueous Sol− Gel Chemistry for Highly Concentrated ZnO-Based Magnetic Semiconductor Nanocrystals. *J. Phys. Chem. C* **2011**, *115*, 1484−1495.
(51) Weakliem, H. A. Optical Spectra of Ni^{2+}, Co^{2+}, and Cu^{2+} in Tetrahedral Sites in Crystals. *J. Chem. Phys.* **1962**, *36*, 2117−2140.
(52) McClure, D. S. Electronic Spectra of Molecules and Ions in Crystals Part II. Spectra of Ions in Crystals. *Solid State Phys.* **1959**, *9*, 399−525.
(53) El Batal, F. H.; El Kheshen, A. A.; Azooz, M. A.; Abo-Naf, S. M. Gamma Ray Interaction with Lithium Diborate Glasses Containing Transition Metals Ions. *Opt. Mater.* **2008**, *30*, 881−891.
(54) McClure, D. S. Optical Spectra of Transition-Metal Ions in Corundum. *J. Chem. Phys.* **1962**, *36*, 2757−2779.

DOI: 10.1021/acs.chemmater.6b05041
Chem. Mater. 2017, 29, 1338−1349

(55) Izumi, K.; Miyazaki, S.; Yoshida, S.; Mizokawa, T.; Hanamura, E. Optical Properties of 3d Transition-Metal-Doped $MgAl_2O_4$ Spinels. *Phys. Rev. B: Condens. Matter Mater. Phys.* **2007**, *76*, 075111.
(56) Yamamoto, T.; Tanaka, T.; Kuma, R.; Suzuki, S.; Amano, F.; Shimooka, Y.; Kohno, Y.; Funabiki, T.; Yoshida, S. NO Reduction with CO in the Presence of O_2 over Al_2O_3-Supported and Cu-Based Catalysts. *Phys. Chem. Chem. Phys.* **2002**, *4*, 2449−2458.
(57) Cavani, F.; Koutyrev, M.; Trifiro, F.; Bartolini, A.; Ghisletti, D.; Iezzi, R.; Santucci, A.; Del Piero, G. Chemical and Physical Characterization of Alumina-Supported Chromia-Based Catalysts and Their Activity in Dehydrogenation of Isobutane. *J. Catal.* **1996**, *158*, 236−250.
(58) Kim, W.; Tachikawa, T.; Majima, T.; Choi, W. Photocatalysis of Dye-Sensitized TiO_2 Nanoparticles with Thin Overcoat of Al_2O_3: Enhanced Activity for H_2 Production and Dechlorination of CCl_4. *J. Phys. Chem. C* **2009**, *113*, 10603−10609.
(59) Al-Zahrani, S. M.; Jibril, B. Y.; Abasaeed, A. E. Selection of Optimum Chromium Oxide-Based Catalysts for Propane Oxidehydrogenation. *Catal. Today* **2003**, *81*, 507−516.
(60) Reddy, B. M.; Rao, K. N.; Bharali, P. Copper Promoted Cobalt and Nickel Catalysts Supported on Ceria−Alumina Mixed Oxide: Structural Characterization and CO Oxidation Activity. *Ind. Eng. Chem. Res.* **2009**, *48*, 8478−8486.
(61) Chen, L.; Horiuchi, T.; Osaki, T.; Mori, T. Catalytic Selective Reduction of NO with Propylene over Cu-Al_2O_3 Catalysts: Influence of Catalyst Preparation Method. *Appl. Catal., B* **1999**, *23*, 259−269.
(62) Maglia, F.; Gennari, S.; Buscaglia, V. Energetics of Aluminum Vacancies and Incorporation of Foreign Trivalent Ions in γ-Al_2O_3: An Atomistic Simulation Study. *J. Am. Ceram. Soc.* **2008**, *91*, 283−290.
(63) Paglia, G.; Božin, E. S.; Billinge, S. J. L. Fine-Scale Nanostructure in γ-Al_2O_3. *Chem. Mater.* **2006**, *18*, 3242−3248.
(64) Paglia, G.; Rohl, A. L.; Buckley, C. E.; Gale, J. D. Determination of the Structure of γ-Alumina from Interatomic Potential and First-Principles Calculations: The Requirement of Significant Numbers of Nonspinel Positions to Achieve an Accurate Structural Model. *Phys. Rev. B: Condens. Matter Mater. Phys.* **2005**, *71*, 224115.
(65) Gutiérrez, G.; Taga, A.; Johansson, B. Theoretical Structure Determination of γ-Al_2O_3. *Phys. Rev. B: Condens. Matter Mater. Phys.* **2001**, *65*, 012101.
(66) Pan, Y.; Liu, C.; Ge, Q. Effect of Surface Hydroxyls on Selective CO_2 Hydrogenation over Ni_4/γ-Al_2O_3: A Density Functional Theory Study. *J. Catal.* **2010**, *272*, 227−234.
(67) Digne, M.; Sautet, P.; Raybaud, P.; Euzen, P.; Toulhoat, H. Use of DFT to Achieve a Rational Understanding of Acid-Basic Properties of γ -Alumina Surfaces. *J. Catal.* **2004**, *226*, 54−68.
(68) Zhou, R. S.; Snyder, R. L. Structures and Transformation Mechanisms of the η, γ and θ Transition Aluminas. *Acta Crystallogr., Sect. B: Struct. Sci.* **1991**, *47*, 617−630.
(69) Wang, Y. G.; Bronsveld, P. M.; DeHosson, J. T. M.; Djuricic, B.; McGarry, D.; Pickering, S. Ordering of Octahedral Vacancies in Transition Aluminas. *J. Am. Ceram. Soc.* **1998**, *81*, 1655−1660.
(70) Lee, M.-H.; Cheng, C.-F.; Heine, V.; Klinowski, J. Distribution of Tetrahedral and Octahedral Al Sites in Gamma Alumina. *Chem. Phys. Lett.* **1997**, *265*, 673−676.
(71) Wang, J. a; Bokhimi, X.; Morales, A.; Novaro, O.; Lopez, T.; Gomez, R. Aluminum Local Environment and Defects in the Crystalline Structure of Sol-Gel Alumina Catalyst. *J. Phys. Chem. B* **1999**, *103*, 299−303.
(72) Pinto, H. P.; Nieminen, R. M.; Elliott, S. D. Ab Initio Study of γ-Al_2O_3 Surfaces. *Phys. Rev. B: Condens. Matter Mater. Phys.* **2004**, *70*, 125402.
(73) Cai, S.-H.; Rashkeev, S. N.; Pantelides, S. T.; Sohlberg, K. Phase Transformation Mechanism between γ- and θ-Alumina. *Phys. Rev. B: Condens. Matter Mater. Phys.* **2003**, *67*, 224104.
(74) Gutiérrez, G.; Taga, A.; Johansson, B. Theoretical Structure Determination of γ-Al_2O_3. *Phys. Rev. B: Condens. Matter Mater. Phys.* **2001**, *65*, 012101.
(75) Wolverton, C.; Hass, K. Phase Stability and Structure of Spinel-Based Transition Aluminas. *Phys. Rev. B: Condens. Matter Mater. Phys.* **2000**, *63*, 024102.
(76) Peng, H.; Li, J.; Li, S.-S.; Xia, J.-B. First-Principles Study of the Electronic Structures and Magnetic Properties of 3d Transition Metal-Doped Anatase TiO_2. *J. Phys.: Condens. Matter* **2008**, *20*, 125207.
(77) Wei, S.-H.; Zhang, S. First-Principles Study of Cation Distribution in Eighteen Closed-Shell $A^{II}B_2^{III}O_4$ and $A^{IV}B_2^{II}O_4$ Spinel Oxides. *Phys. Rev. B: Condens. Matter Mater. Phys.* **2001**, *63*, 045112.
(78) Naumkin, A. V.; Kraut-Vass, A.; Gaarenstroom, S. W.; Powell, C. J. *NIST X-ray Photoelectron Spectroscopy Database*; http://srdata.nist.gov/xps.
(79) Lide, D. R., Haynes, M. W., Eds. *CRC Handbook of Chemistry and Physics, 2009−2010*, 90th ed.; CRC Press/Taylor and Francis, Boca Raton, FL, 2009.
(80) Feng, N.; Wang, Q.; Zheng, A.; Zhang, Z.; Fan, J.; Liu, S.-B.; Amoureux, J.-P.; Deng, F. Understanding the High Photocatalytic Activity of (B, Ag)-Codoped TiO_2 under Solar-Light Irradiation with XPS, Solid-State NMR, and DFT Calculations. *J. Am. Chem. Soc.* **2013**, *135*, 1607−1616.

DOI: 10.1021/acs.chemmater.6b05041
Chem. Mater. 2017, 29, 1338−1349